



Seismicity and structure of Nazca Plate subduction zone in southern Peru



Hobin Lim ^a, YoungHee Kim ^{a,*}, Robert W. Clayton ^b, Clifford H. Thurber ^c

^a School of Earth and Environmental Sciences, Seoul National University, Seoul, 08826, Republic of Korea

^b Division of Geological and Planetary Sciences, California Institute of Technology, Pasadena, CA 91125, USA

^c Department of Geoscience, University of Wisconsin-Madison, Madison, WI 53706-1692, USA

ARTICLE INFO

Article history:

Received 31 January 2018

Received in revised form 5 July 2018

Accepted 10 July 2018

Available online 20 July 2018

Editor: M. Ishii

Keywords:

seismicity
subduction zone system
Nazca Plate
relocation
double-difference tomography
southern Peru

ABSTRACT

We define subducting plate geometries in the Nazca subduction zone by (re)locating intra-slab earthquakes in southern Peru ($14\text{--}18^\circ\text{S}$) and using previously published converted phase analysis results to clarify the slab geometry and inferred relationships to the seismicity. We also provide both P - and S -wave velocity models of the subducting Nazca Plate and mantle layer above the slab using double-difference tomography to understand upper-plate volcanism and subduction zone process. The double-difference constraints for determining the hypocenters and velocity model ensure high accuracy of the relative location of earthquakes with respect to velocity structure. The relocated seismicity shows a smooth contortion in the slab-dip transition zone for ~ 400 km between the shallow (30°)-to-flat dipping interface to the northwest and the 30° -dipping interface to the southeast. We find a significant slab-dip difference (up to 10°) between our results and previous slab models along the profile region sampling the horizontal slab at a depth of $\sim 85\text{--}95$ km. Robust features in both P - and S -wave tomography inversions are both arc-normal and along-arc velocity variations. In the arc-normal direction, all profile results show that the slab velocities beneath the forearc (down to a depth of ~ 100 km) transition to higher velocities beneath the backarc (at $\sim 100\text{--}140$ km depth). In the along-arc direction, velocities of the subducting flat slab are shown to be depressed compared to those of the normal-dip slab. In addition, high shear-wave velocities and low V_p/V_s are detected in the mantle layer above the flat slab, indicating its cold and dry environment. Such differences in the velocity structures for the slab and mantle wedge between the two regions may indicate different hydration states, which greatly affects the upper-plate structure of southern Peru.

© 2018 Elsevier B.V. All rights reserved.

1. Introduction

Along the South American margin between 2°S and 20°S latitude, the Nazca Plate subducts beneath the South American Plate, causing earthquakes, volcanism and upper-plate deformation. Earthquakes in this region exhibit complex rupture characteristics that are related to subducting asperities on the Nazca Plate (Bilek, 2010). In particular, significant subduction-zone complexity in S. Peru has been previously attributed to the moderate-size (~ 200 km \times 18 km) Nazca Ridge and the Nazca fracture zone (Fig. 1). This region includes a transition in slab geometry from flat to normal from north to south (Cahill and Isacks, 1992; Hayes et al., 2012; Phillips et al., 2012; Phillips and Clayton, 2014;

Kim et al., 2015; Ma and Clayton, 2015; Bishop et al., 2017), decrease in magmatic activity towards the flat slab subduction (Ramos and Folguera, 2009), and variability in earthquake rupture patterns and coupling state (Chlieh et al., 2011). The flat slab system developed at 11.2 Ma when the buoyant ridge collided with the forearc at $\sim 11^\circ\text{S}$, and since that time the ridge has been migrating southward (Hampel, 2002). Its present location coincides with the southern end of the flat subduction segment, where the dense seismic arrays are available. In this study, we exploit array data from the Peru Subduction Experiment (PeruSE, 2013) and the Central Andes Uplift and Geophysics of High Topography (CAUGHT; Beck et al., 2010) experiment to better define the subduction zone geometry and constrain the plate boundary dynamics in the slab-dip transition zone at $14\text{--}18^\circ\text{S}$ latitude and at 30–130-km depth (Fig. 1).

Earthquake locations typically provide a first-order estimate of the slab geometry, and by exploiting the relatively long South American earthquake catalog, various groups have constructed

* Corresponding author.

E-mail addresses: hbin7676@snu.ac.kr (H. Lim), younghkim@snu.ac.kr (Y. Kim), clay@gps.caltech.edu (R.W. Clayton), cthruber@wisc.edu (C.H. Thurber).

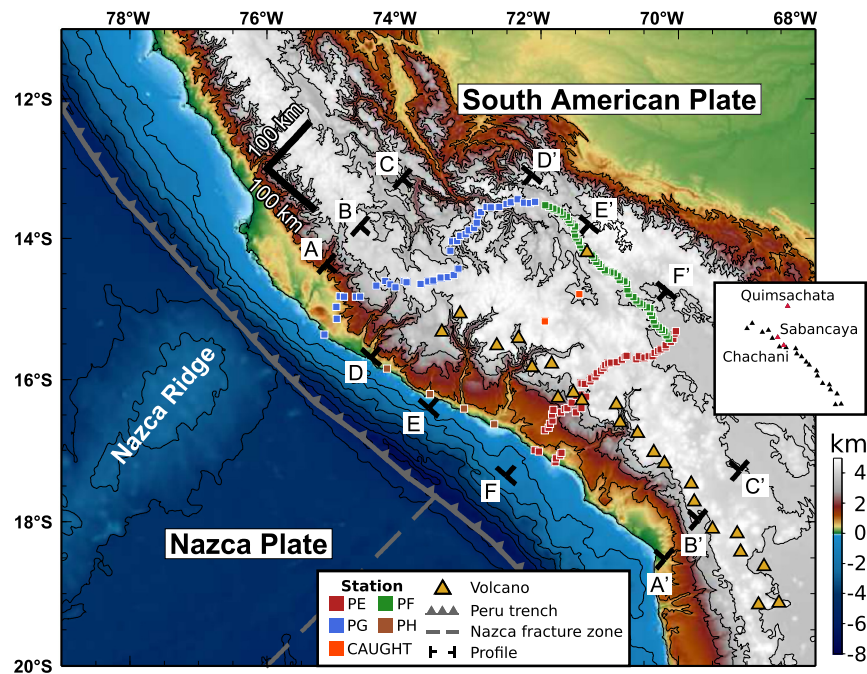


Fig. 1. Topographic–bathymetric map of the study region. Seismic data used in this study are from Peru Subduction Experiment (PeruSE, 2013) and Central Andes Uplift and Geophysics of High Topography (CAUGHT). The topography and bathymetry are contoured with 1000 m interval. Inset indicates the locations of volcanoes Quimsachata, Sabancaya, and Chachani. (For interpretation of the colors in the figure(s), the reader is referred to the web version of this article.)

slab geometry models defined by earthquake locations determined from regional and teleseismic recordings (Figs. 2, 3 and S1–3). The sparsity of the regional seismic network, however, results in a significant disagreement among these models, particularly in the iso-depth contour lines of the Nazca slab at 50 and 100 km, which show the least coherence (Figs. 2, 3 and S1–3). Furthermore, the correlation between the location of the volcanic front and the corresponding slab depth is neither clear nor consistent among the models (Figs. 2, 3 and S1–3). The location of the plate interface beneath the stations is most directly resolved using methods based on teleseismic P -to- S converted phases (Phillips et al., 2012; Phillips and Clayton, 2014; Kim and Clayton, 2015; Ma and Clayton, 2015; Bishop et al., 2017). However, these types of analyses do not constrain the plate geometry between the two linear arrays (PE and PG; Fig. 1) in the region where the horizontally subducting Nazca slab transitions into a normal-dipping slab.

In this study, we focus on the region of flat-slab subduction where the Nazca Ridge subducts; the normal-dip subduction zone south of Nazca Ridge; and most importantly, the region between the two to examine along-strike variations in plate geometry and seismic velocities at depths of 30–130 km. We use regional earthquakes recorded from PeruSE, which consists of three dense seismic array lines surrounding the region between the flat and normal Nazca slab systems and four stations deployed along the coast, and two stations from the CAUGHT network (Fig. 1). Using images based on the relocated seismicity and double-difference tomography (Zhang and Thurber, 2003), we clarify the Nazca Plate geometry and inferred relationships to the subduction process, volcanism in the upper plate, and the occurrence of earthquakes.

2. Data and methods

2.1. Data and initial velocity model

We use the data recorded from the temporary seismic arrays in S. Peru (142 stations from PeruSE and 2 from CAUGHT) from July 2008 to April 2013 (Fig. 1). Interstation spacing of PeruSE is 6–10 km for the PE, PG and PF lines and ~75 km for the PH line

(Fig. 1). We detect local earthquakes using FilterPicker, an automatic picking program that uses multiple frequency bands (Lomax et al., 2012). The program generates over 34 million picks, of which we select only those in which the difference in trigger times is less than the interstation distances divided by the apparent P -wave velocity of 7.0 km/s. Of the 451 earthquakes selected within the study region (Table S1), we manually pick the P wave on vertical-component data and the S on the transverse-component data. The S phase effectively reduces a trade-off between origin time and the depth of intermediate-depth (>100 km) hypocenters.

Initial hypocenters are determined by inverting the arrival times of the P and S phases and using the AK135 velocity model (Kennett et al., 1995) as an initial model. These arrival times are also used to obtain 1-D and 3-D velocity models of the region (see the Supplementary Material). Figs. S4a and b and Table S2 show the optimal 1-D model derived in this study. The hypocenters are then determined based on Markov Chains Monte Carlo method (Myers et al., 2007).

2.2. Double-difference tomography

We apply the double-difference tomography method (Zhang and Thurber, 2003), which jointly inverts, for earthquake hypocenters, P -wave velocity (V_p) and S -wave velocity (V_s). The method minimizes residuals between the observed and calculated arrival times, and the differences between pairs of nearby earthquakes, employing an iterative damped-least-squares method. This method builds on the earthquake location procedure of Waldhauser and Ellsworth (2000), which utilizes the differential times of the P and S phases. 6559 P - and 4145 S -wave arrival times are used in the inversion, and 24,212 differential times measured using waveform cross-correlation are used to constrain the relative locations of the events. Nodes for the inversion are spaced 20 km apart laterally and placed on both the arc-normal trench-perpendicular and along-arc trench-parallel directions (Figs. S4c and d). The nodes are placed at 0, 30 and 50 km in depth for sampling the continental crust, and every 20 km in depth from 70 to 410 km for the mantle wedge and slab (Figs. S4c and d). We determine and apply smooth-

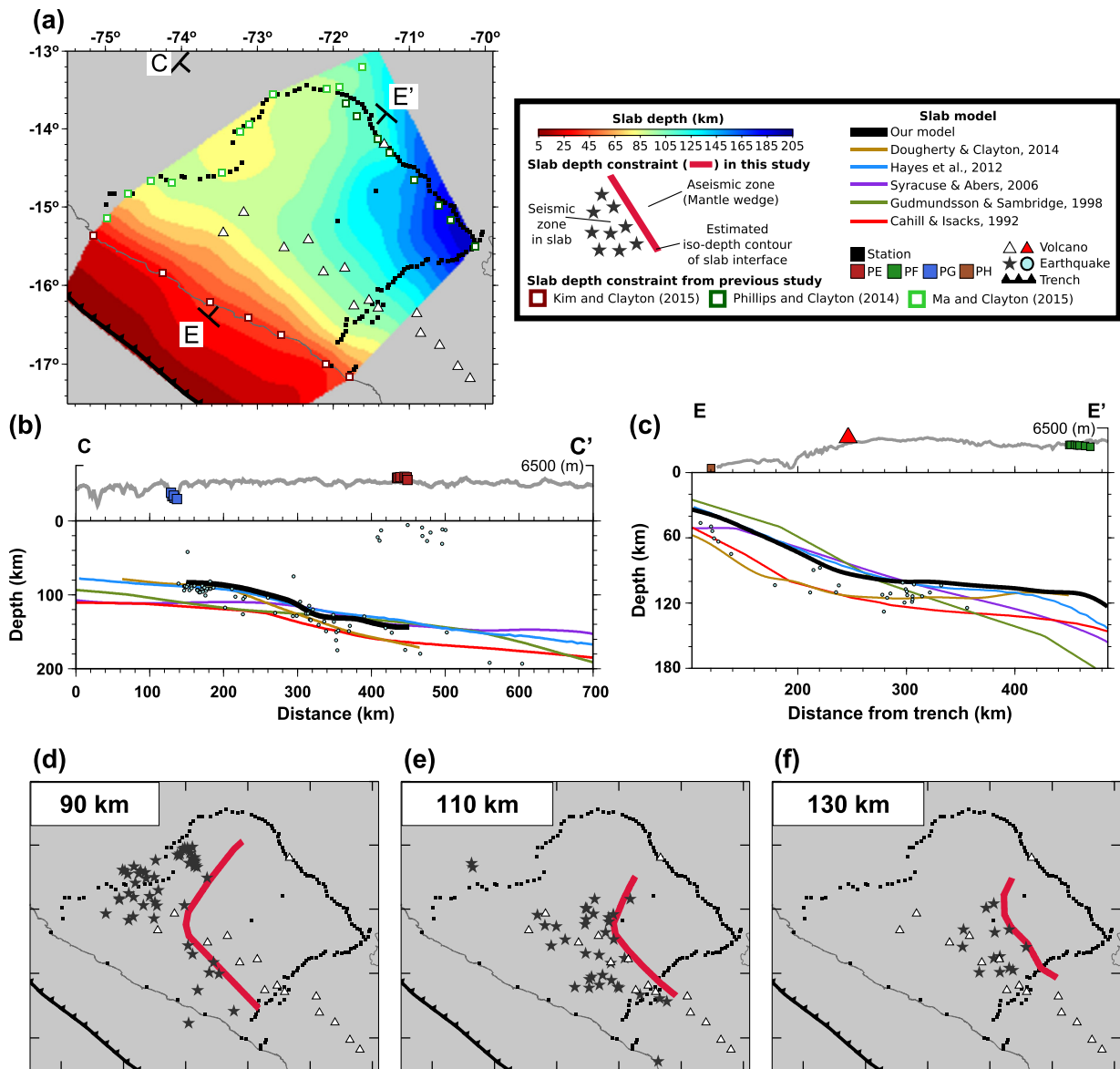


Fig. 2. The model construction for the top slab interface in the slab-dip transition zone and the normal slab-dip zone. (a) Our final slab model. (b) Comparison with previous slab models (see the legend for references) along the trench-parallel profile (C–C' in Fig. 1). (c) Comparison with previous models along the trench-perpendicular profile (E–E' in Fig. 1). The model in the slab-dip transition zone is constrained from the iso-depth contour of the slab interface from the relocated earthquakes at the depth of (d) 90 km, (e) 110 km and (f) 130 km. See Fig. S9 for seismicity plotted on a map view with a depth interval of 5 km.

ing and damping parameters of 8 to stabilize the inversion process (Fig. S4e). The variance reduction for the inversion results shows that its rate of the decrease slows after 11 iterations (Fig. S4f). We then assess the robustness and distribution of the imaged velocity anomalies using checkerboard tests with noise-free data for V_p and V_s in the horizontal and vertical sections (Figs. S5 and S6, respectively).

Lastly, we apply a 2-D and 3-D Gaussian filter to V_p , V_s and V_p/V_s at each inversion node to suppress small-scale heterogeneities. The standard deviations of the Gaussian function for a filter of 10 km-by-10 km and 0.1°-by-0.1° are used for the vertical and horizontal images, respectively, and 14 km for the 3-D visualization. The inversion results for the V_p , V_s and V_p/V_s models without the Gaussian filtering are shown in Fig. S7.

2.3. Construction of a slab geometry model

Our final slab model for the slab-dip transition zone is based on the double-difference algorithm (Zhang and Thurber, 2003). We

incorporate receiver functions to improve the depth resolution of the plate interface in the vicinity of the station arrays because the teleseismic converted phases are sensitive to changes in V_s structure, and hence provide better depth resolution than that of the tomography. Our model shows both horizontal and vertical sections compared to that of previous models (Figs. 2, 3 and S1–S3).

The basis of the model construction is as follows. First we identify seismic and aseismic zones at a depth of 75–115 km (Figs. 2, 3 and S8). We assume that at this depth range earthquakes occur at and below the slab-mantle interface. To constrain the slab geometry in the slab-dip transition zone, the hypocenters within ±3 km from the 90-, 110- and 130-km depth are projected onto the horizontal planes at those depths, and the boundary between the seismic and aseismic zones are manually tracked (Figs. 2d–f). We incorporate the slab-interface depth estimates from the receiver functions along the PF line (Phillips and Clayton, 2014) to constrain the slab depth beyond 130 km in depth. The earthquakes at depths shallower than 90 km are dismissed to avoid ambiguity in distinguishing between intra-slab and crustal earthquakes. For

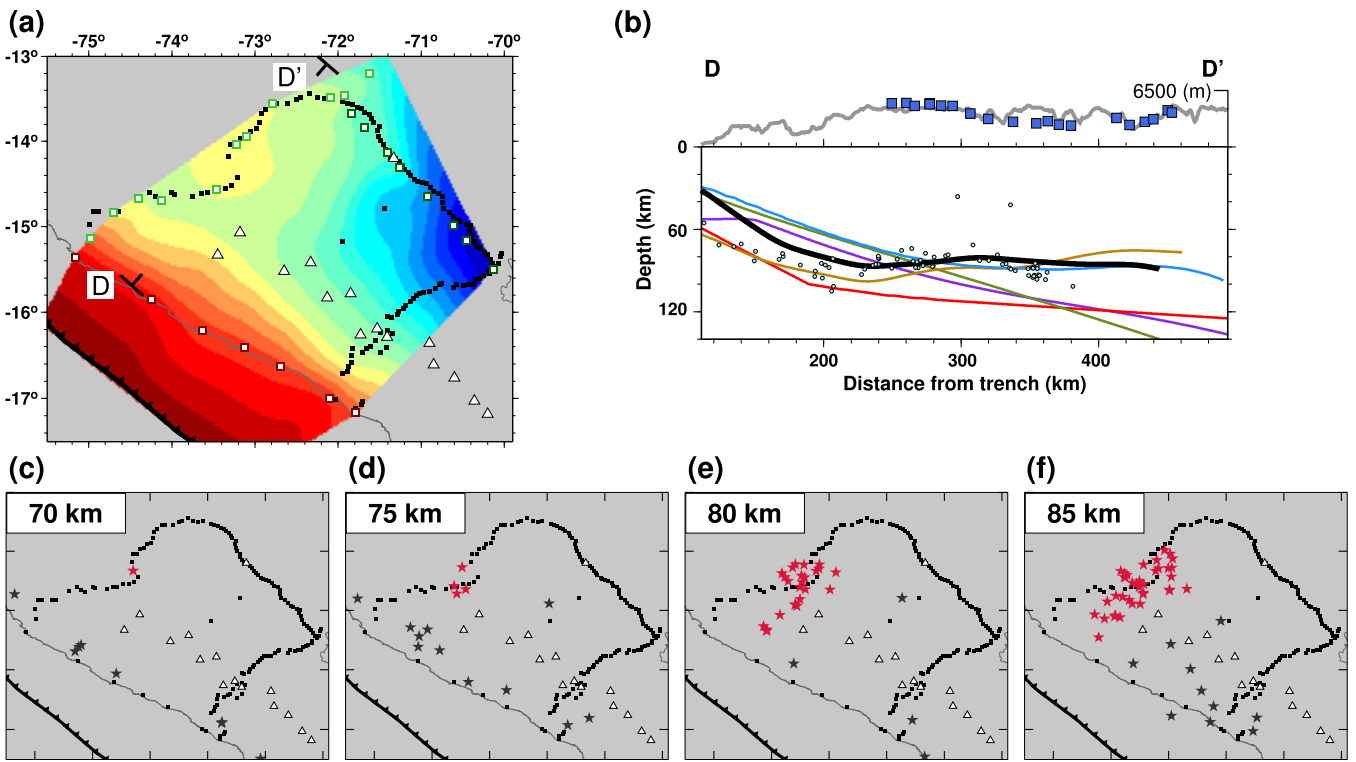


Fig. 3. The model construction for flat slab region. (a) Our final slab model. (b) Comparison with previous slab models (see the legend in Fig. 2 for references) along the trench-perpendicular profile (D-D' in Fig. 1). The slab geometry is constrained by incorporating both receiver function result (Ma and Clayton, 2015) and iso-depth contour based on relocated seismicity with an equal weight on each. The iso-depth contour of the slab interface is obtained from the relocated earthquakes at the depth of (c) 70 km, (d) 75 km, (e) 80 km and (f) 85 km. Red stars indicate earthquakes that are used to constrain the slab geometry at the corresponding depth along the D-D'. See Fig. S9 for seismicity plotted on a map view with a depth interval of 5 km.

the flat-slab region, we incorporate the estimates from the receiver functions along the PG line (Ma and Clayton, 2015) in addition to our seismicity at 70–85 km to achieve enhanced resolution on the slab depth (with an equal weight on each) (Fig. 3). Second, we constrain shallow-depth slab geometries from the trench location (Bird, 2003) and receiver functions for the PH line (Kim and Clayton, 2015). Table S3 shows our slab depth model.

3. Results

We first describe the slab structure derived from the relocated seismicity (Figs. 2 and 3) and then summarize features that are seen in the obtained velocity models using double-difference tomography (Zhang and Thurber, 2003) (Figs. 5–8 and S9–S10). A series of checkerboard resolution tests using more realistic structures based on our slab model (Figs. 2, 3 and S11) in addition to the regular checkerboard pattern of opposite polarities (Figs. S5 and S6) are performed to evaluate the resolution capability of the data set and sensitivity of the models. Fig. 4 demonstrates that the inversion fully recovers a thin (10–20 km) velocity structure.

3.1. Nazca slab geometry based on the double-difference method

3.1.1. Normal-dip slab region

In the normal-dip Nazca slab region, the relocated seismicity extends down to a depth of ~240 km. The normal-dipping segment of the slab (along the profile F-F' of Figs. 5f, 6f and 8f) subducts at a ~30° dipping angle, which is consistent with that of previous models (Figs. S1–3; Cahill and Isacks, 1992; Gudmundsson and Sambridge, 1998; Hayes et al., 2012; Syracuse and Abers, 2006; Dougherty and Clayton, 2014). While the dip of

the slab is similar in all the models in the normal-dip segment, depths to the top slab interface vary, with a difference up to 10 km from our result (Fig. S2f).

3.1.2. Flat slab region

Relocated hypocenters projected to profile D-D' in Figs. 5d, 6d and 8d delineate the horizontally dipping slab. The seismicity extends laterally to ~380 km from the trench and abruptly ceases. The absence of slab seismicity in the region between 71°W and 72.5°W is not an artifact of network coverage because the densely spaced PG-line stations are present near to this region (Fig. 1). Kumar et al. (2016) also observed an absence of seismicity along the projected location of the ridge. The seismicity is elevated by 10–20 km within 14.1°S to 14.7°S (a distance of 240–340 km from the trench) along the profile D-D' (Figs. 5d, 6d, 8d and S2d), as also observed by Dougherty and Clayton (2014) and Ma and Clayton (2015), with a slight difference in the location.

We observe scattered seismicity at 70–100 km depth beneath the PG line, and this can be due to the topographical bulge that we observe (Figs. 5d, 6d, 8d and S2d) and the uncertainty in relocated seismicity (e.g., errors in the manual picking of P and S). Our slab model beneath the PG line (profile D-D') does not exactly follow the seismicity (e.g., Fig. 3b) because a subregion of the slab model beneath the PG line is also constrained using the previous receiver functions (Fig. 3; Ma and Clayton, 2015). Such difference can be attributed to inconsistent velocity model and/or uncertainty of relocated hypocenter. Furthermore, lateral velocity variation within the continental crust and along the top of the slab can also affect depth estimates of the local earthquakes as well as the top plate interface from the receiver function.

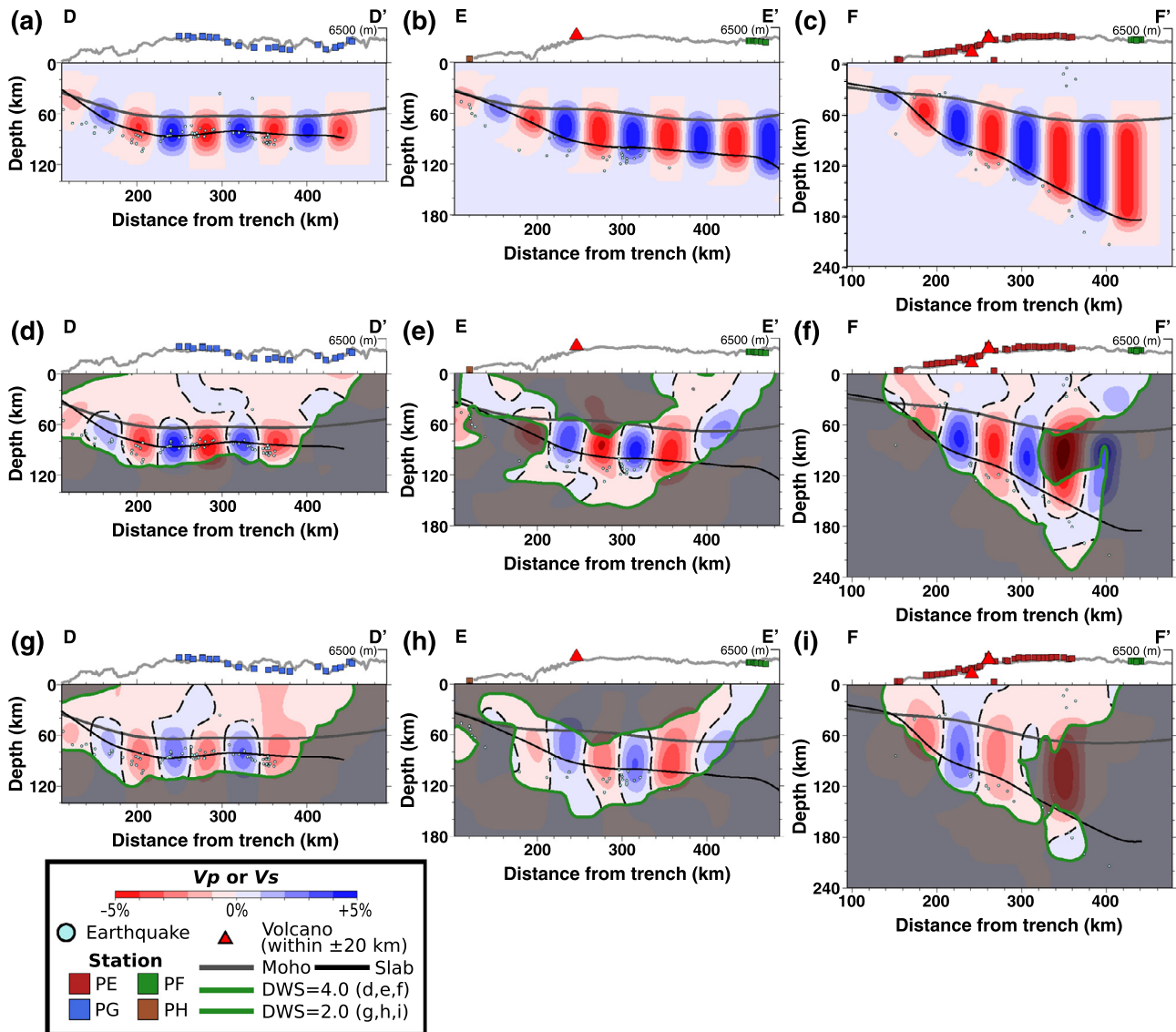


Fig. 4. The recovery test results for the mantle structure between the continental crust (Crust 1.0 model; Laske et al., 2013) and the subducting Nazca slab using our slab model. (a)–(c) Input velocity pattern which constitutes alternating flat cuboids parallel to the trench with $\pm 5\%$ relative velocity. (d)–(i) Recovered V_p (d)–(f) and V_s (g)–(i) models. Images along the profile D–D' (Fig. 1) are shown in (a), (d) and (g), profile E–E' (Fig. 1) in (b), (e) and (h), and the profile F–F' (Fig. 1) in (c), (f) and (i).

3.1.3. Slab-dip region between the normal-dip slab and flat slab

The relocated seismicity delineates the slab-dip transition geometry between the flat and normal subduction zone. The depth variations between the different models are up to 40 km down to 240 km in depth (Fig. S2). Based on the synthetic test and considering the realistic station-source geometry, we obtain an earthquake-depth uncertainty of <10 km in the center of the arrays (Fig. S3).

Along the PG line (profile D–D'), the top slab interface in the subduction-zone backarc is approximately horizontal at a depth of 85–95 km (Figs. 5d, 6d and 8d). The dip of the along-trench slab interface gradually increases towards the SE in the backarc. The transition between the normal and flat slab segments appears smooth based on the seismicity, and we find no sign of a slab tear from the trench to a distance of ~ 420 km and down to a depth of 200 km (Figs. 2, 3 and S2). This is consistent with results based on seismicity (Hasegawa and Sacks, 1981), regression analysis of regional seismicity (Dougherty and Clayton, 2014), and receiver functions (Phillips and Clayton, 2014) along the PF line, sampling the slab-dip transition zone.

3.2. 3-d seismic velocity structure

3.2.1. Synthetic test results

The checkerboard test results for both V_p and V_s in the horizontal slices show that the resolution of the V_p and V_s estimates improves with depth and is stable down to a depth of 130 km (Figs. S5 and S6). In particular, the resolution of the V_p and V_s estimates is good down to a depth of 90 km in examining the slab-dip variation along the trench near the coast (Figs. S5 and S6). The V_s estimates show a similar pattern to that of the V_p estimates (Figs. S5 and S6); however, they show reduced spatial resolution primarily because of the lower number of S-wave phase picks. However, we note that the resolution for V_p and V_s is sufficient in the region that covers both the subducting slab and mantle wedge above the slab. The resolution becomes somewhat limited between 130 km and 220–240 km depth, primarily because of the lack of seismicity at deeper depths.

We next explore more realistic input models and observe how well the inversion recovers them (Figs. 2a, 3a and S11). For this test, we use our slab model as an input, assign a 5% increase in V_p

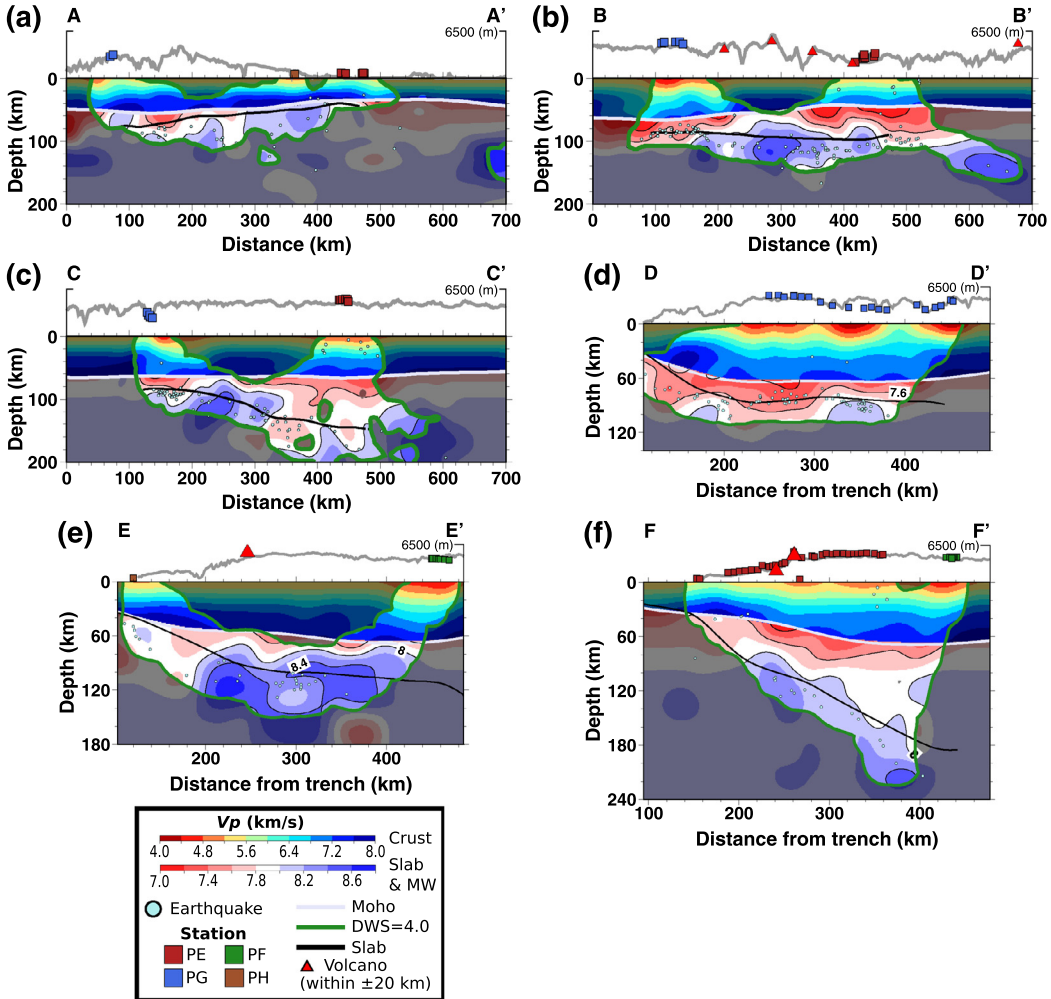


Fig. 5. P -wave velocity in cross-section view along trench-parallel profiles (a) A–A', (b) B–B', and (c) C–C' and arc-normal trench-perpendicular profiles (d) D–D', (e) E–E' and (f) F–F' for which the locations are indicated in Fig. 1. The velocity is moving-averaged from the result of the inversion with Gaussian filter of 10 km and 10 km in the horizontal distance and depth. The top plate interface is retrieved from our slab geometry model in Fig. 2. Moho from Laske et al. (2013). Note that the ray density is separately computed through the derivative weight sum (DWS), which is a weighted measure of the total ray length close to a node in the inversion grid. The DWS is set as 4 for P -wave data. See Supplementary Data for details.

and V_s with respect to the initial 1-D model for the slab and test how sensitive the inversion is to the slab velocity structure. We note that the absence of a high-velocity anomaly along the flat slab region at 90 km (Fig. S11) represents a case for a topographical bulge on the slab, which is shown by the seismicity (Figs. 3b). The seismicity is elevated by 10–20 km from the horizontal plane (also noted in Section 3.1.2). We observe that an inversion recovers the fast-velocity anomaly reasonably well at a depth range of 50–110 km for both V_p and V_s (Fig. S11). The high-velocity anomaly for the flat slab in the backarc at 90 km is not well recovered (Fig. S11).

We then construct a model based on our slab geometry (Figs. 2 and 3) and examine how sensitive the inversion is to the mantle-wedge velocity structure. Our slab model (Figs. 2 and 3), as well as receiver functions (Ma and Clayton, 2015; Bishop et al., 2017), indicate that the mantle layer is quite thin (<20 km) between the overriding plate and the slab in the flat-slab region. We observe that the inversion is sensitive to a thin (10–20 km) structure, and the velocity recovery is moderate with noticeable vertical smearing in all profile images (Fig. 4).

3.2.2. P -wave velocity structure

The inversion results of V_p are presented with the top slab interface in Figs. 5, S7a and S9. The estimates of nodes with sufficient ray coverage are enclosed by a green line in the figures.

Figs. 5 and S9 show the absolute value of V_p from the inversion in the vertical cross-section and horizontal slice views, respectively. Fig. S7a shows the inversion results in a horizontal slice without Gaussian filtering.

Several structural elements related to the Nazca slab and mantle layer can be identified from the inversion results. The V_p estimates for the slab (the imaged region below the top plate interface) down to a depth of 200 km along all profiles vary significantly in the vertical and lateral (arc-normal) directions, and overall show values between 7.4 to 8.6 km/s (Figs. 5 and S9). In the arc-normal direction, all profile results show that the slab velocities beneath the forearc (down to a depth of 100 km) transition to higher velocities beneath the backarc (at a depth of 100–140 km). In the arc-parallel direction, we also observe relatively a low V_p within the slab along the profile D–D' and profile F–F', and a high V_p in between (profile E–E'). In particular, high V_p estimates (8.0–8.6 km/s) are observed along profiles B–B' (distance 180–420 km; Fig. 5b) and C–C' (190–350 km; Fig. 5c). Low V_p estimates (7.4–8.0 km/s) are observed along profiles A–A' (40–200 km at 7.4–8.0 km/s; Fig. 5a), B–B' (40–180 km at 7.4–8.0 km/s and 440–540 km at 7.8–8.0 km/s; Fig. 5b) and C–C' (100–180 km at 7.6–8.0 km/s and 320–480 km at 7.6–8.0 km/s; Fig. 5c).

The mantle layer corresponds to the imaged region between the base of the continental crust (Laske et al., 2013) and the

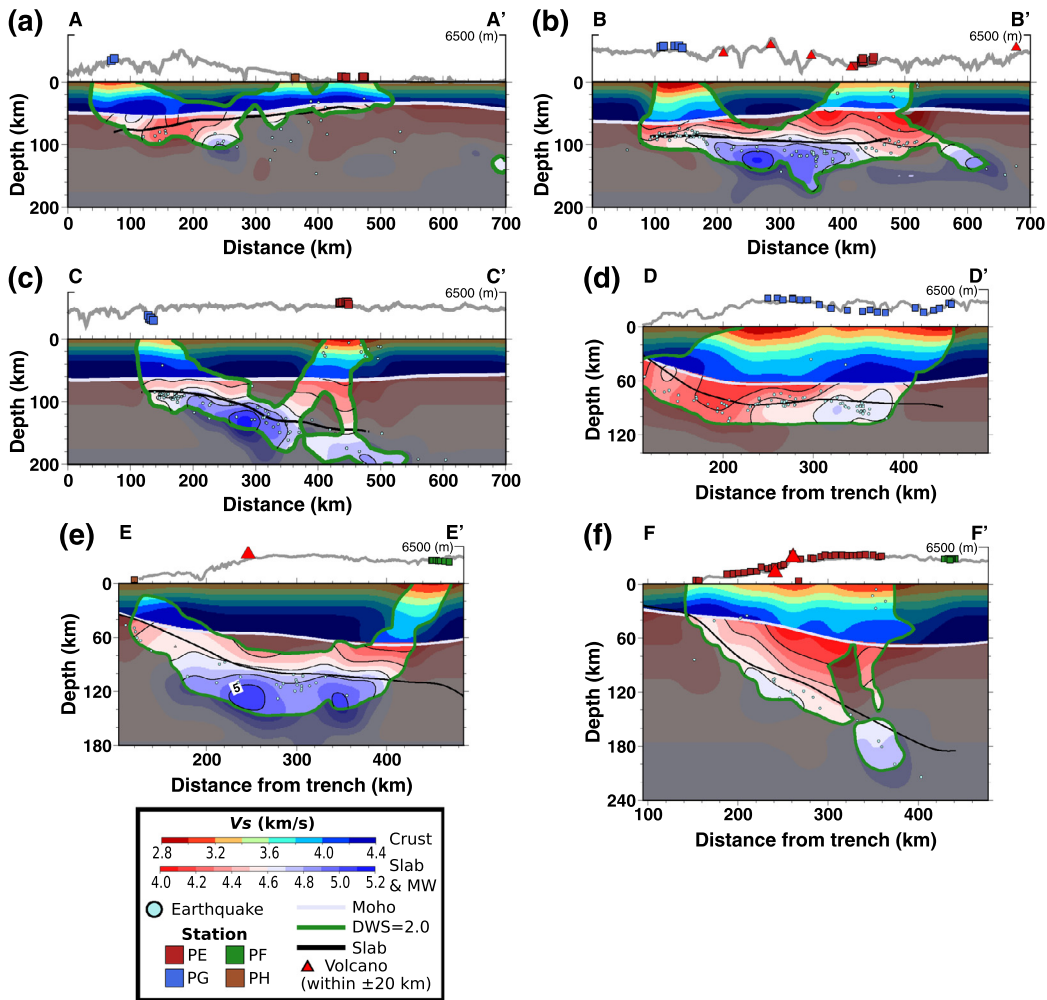


Fig. 6. S-wave velocity in cross-section view along trench-parallel profiles (a) A-A', (b) B-B', and (c) C-C' and arc-normal trench-perpendicular profiles (d) D-D', (e) E-E' and (f) F-F' for which the locations are indicated in Fig. 1. The velocity is moving-averaged from the result of the inversion with Gaussian filter of 10 km and 10 km in the horizontal distance and depth. The top plate interface is retrieved from our slab geometry model in Fig. 2. Moho from Laske et al. (2013). Note that the DWS is set as 2 for this S-wave data. See Supplementary Data for details.

top slab interface defined in our model (Figs. 2 and 3). The V_p of the forearc mantle ranges from 7.2 km/s to 8.0 km/s (Fig. 5). The V_p above the flat slab in the forearc is 7.2–7.6 km/s (distance 170–220 km; Fig. 5d), 7.4–8.0 km/s in the slab-dip region (160–230 km; Fig. 5e), and 7.6–8.0 km/s in the normal-dip region (160–230 km; Fig. 5f). The V_p of the backarc mantle ranges from 7.4 to 8.4 km/s (Fig. 5). The V_p above the flat slab in the backarc is 7.4–7.7 km/s (330–400 km; Fig. 5d), 7.8–8.4 km/s in the slab-dip region (260–420 km; Fig. 5e), and 7.2–7.8 km/s in the normal-dip region (270–380 km; Fig. 5f).

3.2.3. S-wave velocity structure

The inversion results of V_s are presented in Figs. 6, 7, and S7b. Figs. 6 and 7 show the absolute value of V_s from the inversion in vertical cross-section and horizontal slice views, respectively, and Fig. S7b shows a horizontal slice view without Gaussian filtering. The spatial resolution of the recovered V_s is slightly less compared to the results of V_p , as also observed in the checkerboard test results (Figs. S5 and S6). Regardless, we observe broadly similar patterns in the V_p results.

Similar to the V_p estimates, we observe a relatively low V_s within the slab beneath the PG (profile D-D') and PE (profile F-F') lines, and high V_s in between (profile E-E'). High V_s estimates (4.6–5.1 km/s) are obtained along profiles B-B' (distance 180–420 km; Fig. 6b) and C-C' (190–350 km; Fig. 6c). Low V_s esti-

mates (4.2–4.6 km/s) are observed along profiles A-A' (40–200 km at 4.2–4.6 km/s; Fig. 6a), B-B' (40–180 km at 4.2–4.6 km/s and 440–540 km at 4.2–4.6 km/s; Fig. 6b) and C-C' (100–180 km at 4.4–4.6 km/s and 320–480 km at ~4.6 km/s; Fig. 6c). These velocity anomalies are also observed along three trench-perpendicular profiles (Figs. 6d–f). In addition, our V_s values at the dipping-slab segment at 90 km in depth (profile D-D') agree well with previous estimates (Ma and Clayton, 2014; Ward et al., 2016).

The V_s of the forearc mantle ranges from 4.2 km/s to 4.6 km/s (Fig. 6). The V_s above the flat slab in the forearc is 4.2–4.3 km/s (distance 170–220 km; Fig. 6d), 4.5–4.6 km/s in the slab-dip region (160–230 km; Fig. 6e), and 4.3–4.5 km/s in the normal-dip region (160–230 km; Fig. 6f). The V_s of the backarc mantle ranges from 4.0 to 4.7 km/s (Fig. 6). The V_s above the flat slab in the backarc is 4.5–4.7 km/s (330–400 km; Fig. 6d), 4.4–4.6 km/s in the slab-dip region (260–420 km; Fig. 6e), and 4.0–4.3 km/s in the normal-dip region (270–380 km; Fig. 6f).

3.2.4. P-to-S wave velocity ratio (V_p/V_s) structure

V_p/V_s is obtained by taking the ratio of the V_p and V_s estimates retrieved from the inversion. We note that in the inversion the P- and S-wave travel times are inverted simultaneously with the same damping factor. The resulting ray coverage for V_p/V_s is different from that of the V_p estimates because the number of S-wave arrival times is less than that for the P-wave. Because of

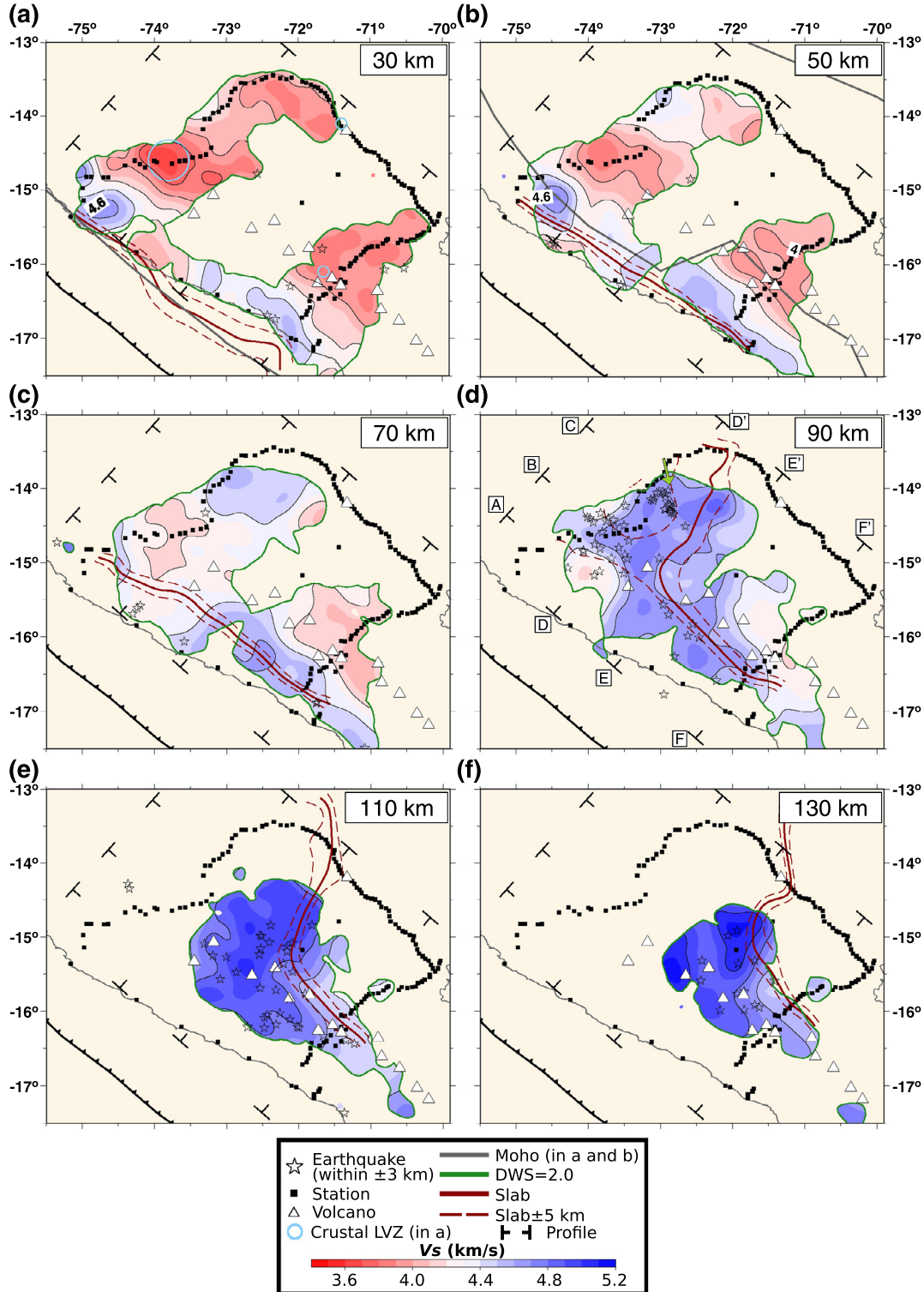


Fig. 7. Horizontal slices of S -wave velocity at depths (a) 30, (b) 50, (c) 70, (d) 90, (e) 110 and (f) 130 km. The Gaussian filter with standard deviation of 0.1° -by- 0.1° is applied for simplicity. LVZ—Low velocity zone. An arrow in a panel (d) indicates the region where we observe no slab seismicity at 71°W and 72.5°W longitude.

differing data quality and distribution between the P and S data, Vp/Vs estimated from Vp and Vs can be difficult to interpret (Zhang and Thurber, 2003). Regardless of such a limitation, Vp/Vs provides an important constraint on the physical state of the imaged structure (i.e. the mantle wedge) in terms of temperature and/or composition. Our estimates for Vp/Vs are presented in vertical and horizontal slice views in Figs. 8 and S10, respectively, and Fig. S7c shows a horizontal slice view without Gaussian filtering.

The Vp/Vs from the inversion shows an approximately similar pattern to values obtained for Vp and Vs (Fig. 8). The Vp/Vs of the forearc mantle ranges from 1.65 to 1.80 (Fig. 8). The Vp/Vs estimates above the flat slab in the forearc are 1.70–1.80 (distance 170–220 km; Fig. 8d), 1.65–1.75 in the slab-dip region (160–230 km; Fig. 8e), and 1.70–1.80 in the normal-dip region (160–230 km; Fig. 8f). The Vp/Vs of the backarc mantle ranges from 1.60 to 1.90 (Fig. 8). The Vp/Vs above the flat slab in the backarc

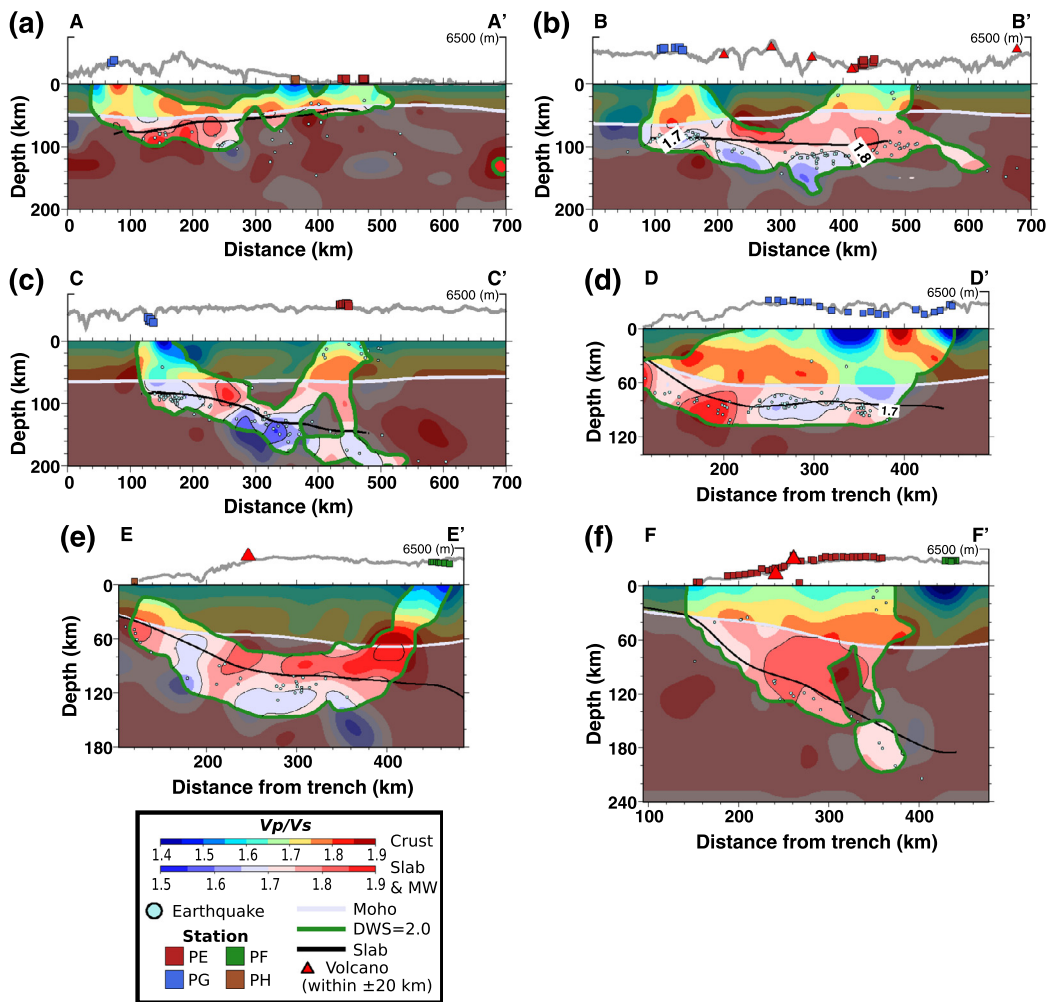


Fig. 8. V_p/V_s in cross-section view along trench-parallel profiles (a) A–A', (b) B–B' and (c) C–C' and arc-normal trench-perpendicular profiles (d) D–D', (e) E–E' and (f) F–F' for which the locations are indicated in Fig. 1. The velocity is moving-averaged from the result of the inversion with Gaussian filter of 10 km and 10 km in the distance and depth. The top plate interface is retrieved from our slab geometry model in Fig. 2. Moho from Laske et al. (2013). Note that the contour of the DWS is same with that in the V_s . See Fig. F8 for the V_p/V_s estimates in a horizontal slice. See Supplementary Data for details.

is 1.60–1.70 (330–400 km; Fig. 8d), 1.80–1.90 in the slab-dip region (260–420 km; Fig. 8e), and 1.80–1.85 in the normal-dip region (270–380 km; Fig. 8f).

3.2.5. Crustal low-velocity zones

We identify several localized crustal low-velocity zones along different profiles beneath the PE, PF and PG lines (profiles F–F', C–C' and D–D', respectively; Figs. 9a and S12). We confirm this as a low-velocity feature from the filtered seismic phases of the local earthquakes (Figs. 9 and S12). The waveform record sections show either attenuated amplitudes of S phases or a complicated body-wave coda for waves passing through those zones (Figs. 9 and S12).

The most prominent low-velocity zone is imaged beneath stations PG16–PG27 (Fig. 9). The V_s estimates are <3.6 – 3.8 km/s, which are a <8 – 10% reduction with respect to our 1-D model. Ma and Clayton (2015) also detected this low-velocity zone from teleseismic P -to- S converted phases. Based on our results (considering 3.8 km/s contour values and less), its approximate dimension is ~ 60 km (arc-normal direction) by ~ 100 km (along-arc direction). The waveform record of one crustal earthquake at a depth of 30 km near the PG line shows a clear difference in amplitude of the S phase between the waveforms from the stations PG15–PG26 and PG28–PG45 (Fig. 9b). The amplitudes from sta-

tions PG15–PG26 appear to be substantially attenuated, and their raypaths pass through the low-velocity zone.

In addition, we observe a low-velocity zone (V_s of ~ 3.8 km/s; 8% reduction beneath volcanoes; Sabancaya and Chachani; Fig. 1) along the PE line in a 30 km depth slice (Fig. S12a and b). The spatial dimension of this zone is ~ 30 km based on the velocity contour (Fig. 7a), and it is coincident with a scatterer location that was discussed in an ambient noise cross-correlation study (Ma et al., 2013). Another low-velocity zone (V_s of <3.8 km/s) is observed beneath and near Quimsachata volcano (Fig. 1), which is ~ 160 km from the volcanic front (Fig. S12c and d). The waveform record section along the PF line from a deep earthquake shows more complicated S arrivals for stations PF32 and PF33, which pass through this crustal low-velocity zone (Fig. S12d). Its corresponding lateral dimension is estimated to be ~ 5 km or less (Fig. S12c).

4. Discussion

In this study, we define the slab geometry down to a depth of 130 km by relocating the seismicity with the highest resolution and examine the slab-dip velocity transition using the inversion based on the double-difference algorithm. The tomography jointly inverts velocities and hypocenters and thus enables one to compare velocity anomalies directly using seismicity. There is a discrepancy between the velocity and hypocenter unless they are

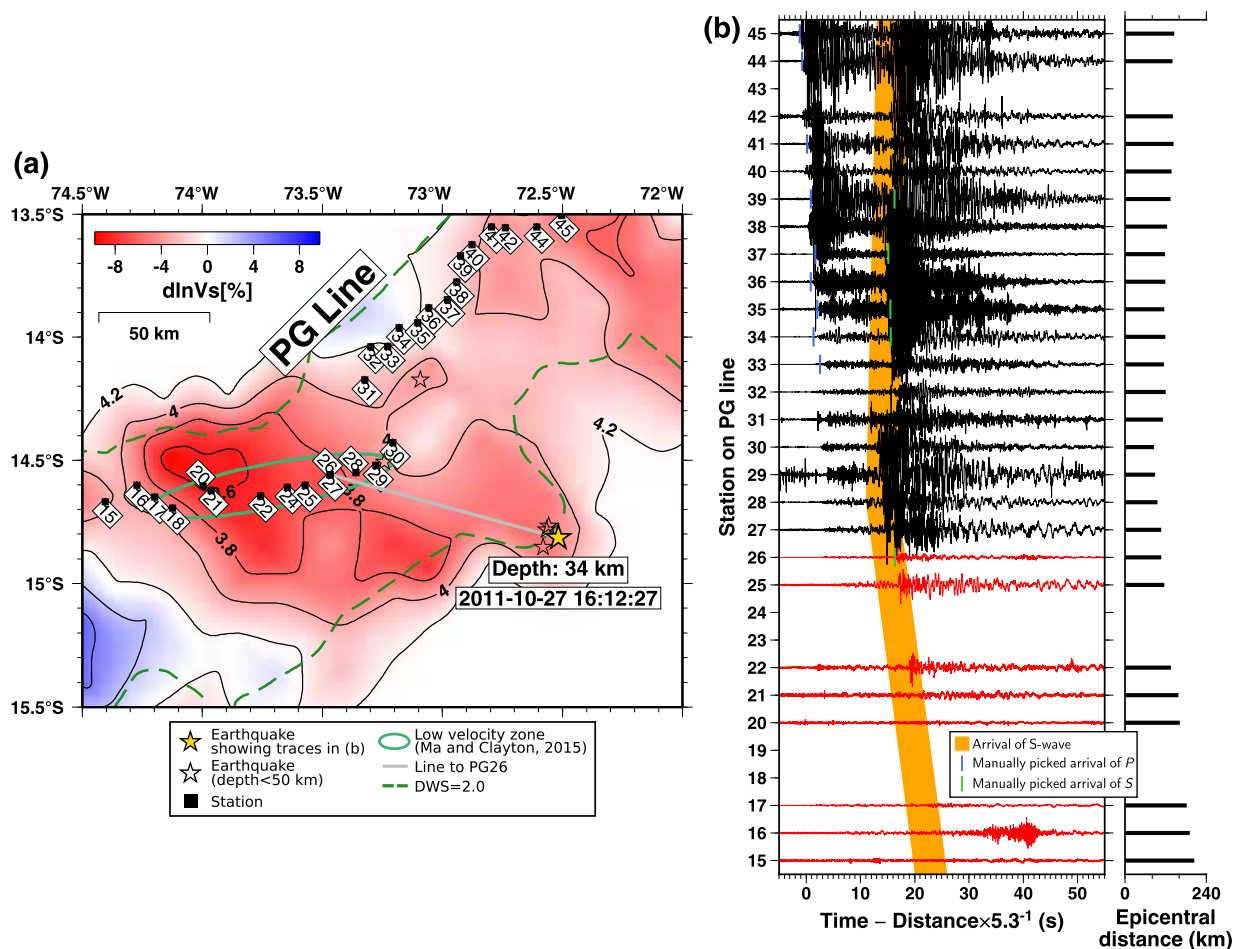


Fig. 9. Presence of crustal low-velocity zone (LVZ) on the normal-dip subduction zone at a depth of 30 km along the PG line. (a) S-wave velocities without Gaussian filtering at 30 km depth along the PG line. (b) Transverse-component record section of the local earthquake recorded from the PG stations. The highpass filter is applied at 0.25 Hz. A thick orange line in the record section highlights the sudden change in amplitude of S phase, which indicates different path effects due to the LVZ within the continental crust. Traces from stations PG15–PG26 are indicated in red, and their amplitudes are substantially attenuated. See Fig. S11 for other LVZs along the PE and PF lines.

based on the same velocity model. Because the structural feature that we image can be quite thin (i.e. a <20-km-thick mantle layer above the flat slab; Fig. 4), a slight error in earthquake locations can lead to erroneous interpretation.

4.1. Nazca slab geometry based on seismicity

4.1.1. Flat slab region

In the flat slab region, the Nazca slab subducts at a 30° dipping angle down to 85–95 km depth, and then transition into generally flat geometry for ~ 200 km (Fig. 3). Although our model domain is limited to a distance of ~ 400 km from the trench, the flat slab extends further inland for approximately 100 km based on receiver functions (Phillips and Clayton, 2014; Ma and Clayton, 2015). We observe topographical bulge on the slab, elevated by ~ 10 –20 km from the slab surface at the localized zone (14.1° – 14.7° S) (Figs. 3, 5d, 6d and 8d). Given this observation, the slab geometry following the topography of the continental Moho (Ma and Clayton, 2015) probably indicates the presence of an enhanced slab suction force (Tovish et al., 1978).

Although there are many factors contributing to the flat-slab development in Peru (e.g., Manea et al., 2017), the seismological evidence suggests that suction force plays an important role in maintaining the flat plate geometry in the vicinity of the subducting ridge because its buoyancy alone cannot fully explain the slab-flattening process (Kim and Clayton, 2015; Ma and Clayton, 2015). The constriction of the mantle layer between the flat slab

and continental crust inhibits typical asthenospheric corner flow, leading to a large negative pressure that further decreases the dip angle of the slab (Ma and Clayton, 2015). The presence of a thick (Ryan et al., 2016; Bishop et al., 2017) and cold continental lithosphere (Currie and Hyndman, 2006) may act as a partial barrier to the mantle-wedge flow, resulting in a decreased pressure in the mantle-wedge corner (O'Driscoll et al., 2012).

The decreasing dip of the slab certainly indicates a decreasing influx of asthenospheric mantle above the slab. As a result, the slab flattening process significantly cools the system, particularly the upper lithosphere (e.g., Ramos et al., 2002), and a decreasing degree of partial mantle melting is expected at the arc location eventually shutting off arc magmatism in the flat slab region. Our seismicity results show that locations of the volcanoes correspond to the 85–105 km iso-depth contour of slab-surface beyond the flat slab region towards the SE (Figs. 2 and 3).

4.1.2. Slab-dip transition zone

The relocated seismicity shows a smooth contortion in the slab-dip transition zone for ~ 400 km between the 30° -to-horizontal dipping interface to the NW and 30° -dipping interface to the SE. This slab-dip transition zone is currently under an extensional stress regime based on the N-S and NW-SE extensional mechanisms of the regional earthquakes (Dougherty and Clayton, 2014). Based on our seismicity, we do not observe any sign of slab tear including upwelling of sub-slab asthenosphere (Figs. 2, 3 and S1–2). The slab is estimated to have experienced 10% strain in the

along-strike direction across this transition (Dougherty and Clayton, 2014).

We note that our study has an adequate resolution down to a depth of about 240 km (Figs. 5, 6 and 8) for interpreting features associated with the dipping slab and mantle in the vicinity of the subducting slab. The teleseismic tomography study by Scire et al. (2016) covers a larger spatial region with a deeper depth resolution from ~100 km to 660 km and shows a similar slab-dip transition zone from shallow (flat) subduction in the northern area to more normal dipping subduction to the south. In particular, their results show the transition from horizontally dipping to steeply dipping (~70°) in the flat slab region. This region of the slab steepening corresponds with the predicted edge of the subducted Nazca Ridge, implying that the geometry of the Nazca slab is at least locally influenced by the presence of the ridge (Scire et al., 2016).

4.2. Seismic velocity variation based on tomography

The images of the V_p , V_s and V_p/V_s structures of the dipping slab are interpreted simultaneously with seismicity because these measurements provide different types of constraints and the use of all four structures can reduce ambiguity in interpretation. The velocities, particularly V_p/V_s , and earthquake locations are important for discussing variations in temperature and/or composition of the slab and also the mantle layer above the slab.

4.2.1. Nazca slab velocity variation

A relatively higher-velocity slab is imaged along all profiles examined (Fig. 1), and the velocity variations are substantial in the arc-normal and along-arc directions (Figs. 5, 6 and 10a). The images along the arc-normal profiles show that the velocities of the slab in the backarc are elevated compared to those in the forearc. Such an arc-normal change in velocities can be attributed to a mineral phase change (e.g., eclogitization) within the subducted crust (Peacock, 2004). Typically, teleseismic converted phases at the top of the slab can sharply constrain the basalt-to-eclogite transition and associated slab dehydration along the slab interface. In the normal slab-dip region, such converted signals at the top plate interface disappear at depth of ~100 km in S. Peru (Phillips et al., 2012) and 120 km in the central Andes (Yuan et al., 2000). In the flat-slab system, converted signals are well observed down to a depth of ~80 km and up to ~500 km from the coast (Phillips and Clayton, 2014; Ma and Clayton, 2015). Although tomography cannot sharply constrain the depth of the eclogitization, the observed arc-normal velocity variation (increasing velocities towards the backarc) can be somewhat constrained by the petrological transition because of changes in pressure (P) and temperature (T) conditions within the slab.

In the along-arc profiles, the flat slab is associated with relatively lower velocities than those of the slab-dip and the normal-dip slab regions (Figs. 5, 6 and 10a), which is consistent with the converted phase analysis results (Kim and Clayton, 2015). The flat portion of the upper part of the oceanic crust was shown to be more fluid-rich than the normal-dip region by Kim and Clayton (2015). They observed considerable V_s reductions of ~20–40% near the top plate interface of the flat slab at ~40–120 km depths (which is ~10–20% lower than the estimates for the normal slab-dip region). In fact, such velocities are far lower than expected for unaltered mid-ocean ridge basalt (MORB) or gabbro in the appropriate region of P - T conditions at that depth (Hacker et al., 2003), and cannot be fully explained without the presence of fluid (Kim and Clayton, 2015). Considering such a different hydration degree between the flat and normal slabs, the subduction of the ridge could be a critical factor in the supply of the fluid into the system (Kim and Clayton, 2015). Also, it may be that the subduction

of the ridge retards the phase transition to a denser mineral (e.g., eclogite), and ultimately contributes to the buoyancy of the flat slab. The retardation of the phase transformation (i.e. the basalt-to-eclogite conversion) in the oceanic crust is also supported by weakened P -to- S converted signals (Bishop et al., 2017).

The 90 km-depth slice from our inversion (Fig. 7d) shows the clearest image of the slab geometry. A faster V_s (4.5–4.6 km/s; Fig. 7d) corresponds to (1) a flat-slab segment with intense in-slab seismicity along the PG line (profile D–D') and (2) a dipping-slab segment in both the slab-dip transition and normal-dip zones that extends 250 km from the trench. Such high velocities and the pervasive presence of earthquakes in this high V_s region confirm the presence of the Nazca slab at 90 km depth along the PG line (profile D–D'). A slightly lower V_s (4.3–4.4 km/s) is also obtained in the flat slab region at the same depth (Fig. 7d). Earthquakes occur in the vicinity of this low V_s region. It appears that the velocities of the flat slab below the top plate interface laterally vary, and thus this observation points to the heterogeneous nature of the flat slab, which could be closely related to the phase transition and possibly influenced by the subducting ridge. Antonijevic et al. (2015) discussed low-velocity features in the NW region of the ridge (beyond our study region) as a possible slab tear. The relocated seismicity in this study is not consistent with a slab tear (Figs. 6d and S8).

4.2.2. Velocities and V_p/V_s of the mantle layer above the Nazca slab

Upon subduction, the fluids are released from the subducting slab in a series of metamorphic reactions, and the flux into the mantle wedge modifies its chemical and physical properties. Such subduction-related hydration plays a significant role in controlling V_s within the upper oceanic crust and overlying mantle wedge, as evidenced in Kim and Clayton (2015) and Ma and Clayton (2015) for S. Peru, and from the studies in central Mexico (Kim et al., 2013) and central Chile (Porter et al., 2012). The hydration process within the forearc mantle is closely related to serpentinization, which can drastically reduce the seismic velocity and density of the mantle while increasing Poisson's ratio (and V_p/V_s) (Hyndman and Peacock, 2003).

Generally depressed velocities and elevated V_p/V_s in the forearc mantle (Figs. 5, 6, 8 and 10b) indicate an overall low degree of serpentinization in S. Peru, compared to estimates from other subduction zones (e.g., Alaska–Aleutians (10–20%) and Cascadia (<50–60%) beneath forearc and/or active arc) (Hyndman and Peacock, 2003). The low degree of serpentinization in S. Peru can be attributed to slow dehydration of the slab because of relatively old age of the oceanic plate (Abers et al., 2017). The degree of serpentinization in the flat slab, the slab-dip and the normal-dip regions are 10–30%, 0–20% and 5–15%, respectively (Hyndman and Peacock, 2003). Relatively higher degree of mantle serpentinization in the flat slab region than that in the other regions can be attributed to hydrous compositions in the subducting ridge and metasediments (Kim and Clayton, 2015).

The key features in our velocity models are the relatively high V_s (4.5–4.7 km/s) and low V_p/V_s (1.60–1.70) in the thin mantle layer above the flat slab in the backarc (Figs. 6, 8 and 10b). In the flat slab region, Currie and Hyndman (2006) mentioned the presence of a notably cool backarc mantle. Ma and Clayton (2015) also imaged the high-velocity mantle above the initial half of the flat slab and normal velocity values on the remainder of the flat-slab segment. Similar values to ours are observed in central Chile, where the Juan Fernandez Ridge is subducting (Porter et al., 2012), and Wagner et al. (2006) suggested that the high V_s (4.6–4.7 km/s) and low V_p/V_s (1.64–1.74) above the central Chile–Argentina flat slab cannot be modeled using any hydrated composition. In both flat-slab systems where the ridge subduction is involved, the composition of the mantle is probably enhanced by the region's low geotherm, and point to seismic properties of dry Mg-rich peridotite

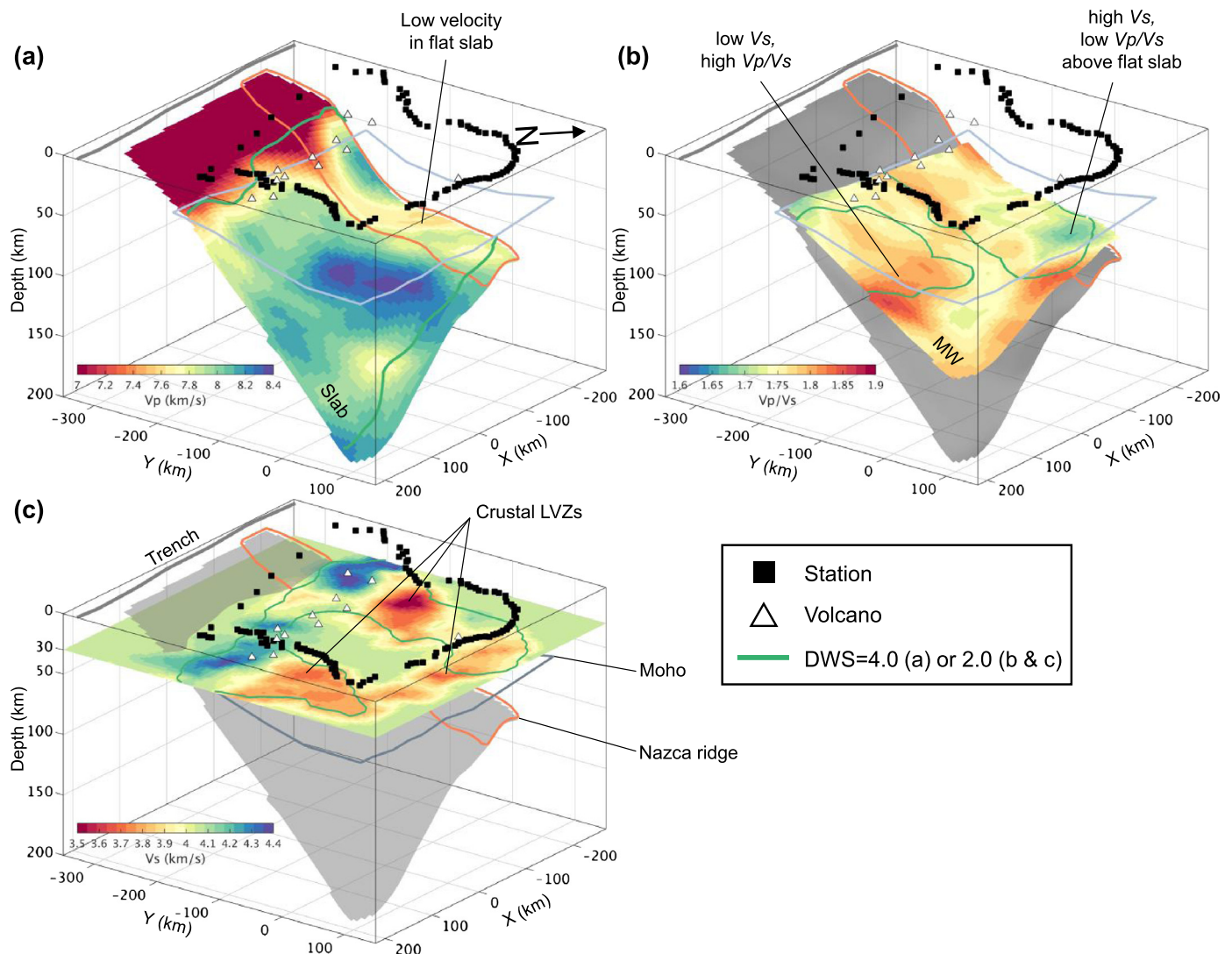


Fig. 10. 3-D diagram of Nazca Plate subduction system based on our tomographic models. (a) V_p structure for Nazca slab which is sliced at 5 km below the top plate interface from our slab model. (b) V_p/V_s structure for mantle layer above the subducting slab. (c) V_s crustal structure at 30 km depth slice. Note that there is a vertical exaggeration. The approximate shape and location of the Nazca Ridge are taken from Hampel (2002). 3-D Gaussian filter is applied to (a) and (b) before slicing velocity models. Moho from Laske et al. (2013). LVZ—Low velocity zone. MW—Mantle wedge (layer).

and orthopyroxene enrichment (e.g., Wagner et al., 2006, 2008; Qian et al., 2018). For orthopyroxene enrichment in the mantle, a large quantity of silica must be added to the mantle (Wagner et al., 2008) and the source for this silica would be the metasediments and subducted crust (Nazca Ridge) in S. Peru (Kim and Clayton, 2015). This process coincides well with the cessation of arc volcanism at the surface.

We note that our velocity and V_p/V_s estimates can be alternatively explained by the anisotropy of the mantle peridotites (Hacker and Abers, 2012). Our estimates can be biased by anisotropy in mantle rock fabric or by the raypaths through the mantle, leading to relatively high V_s and/or low V_p compared with isotropic averages (Hacker and Abers, 2012). Local S-wave splitting measurements suggest that mantle above the flat slab appears to be anisotropic, with ~4% anisotropy in a ~30 km-thick mantle layer (Eakin et al., 2014). This anisotropy estimate is explained by the lattice-preferred orientation of olivine (Eakin et al., 2014), and thus we cannot rule out the possibility for the contribution of seismic anisotropy to our estimates.

The observed low V_s (4.0–4.3 km/s) and high V_p/V_s (1.80–1.85) above the normal-dip slab in the backarc indicate partially molten state of the mantle, which can be attributed to the arc magma-

tism. The temperature of the subarc mantle is 1100–1300 °C at 60–120 km in depth (Currie and Hyndman, 2006).

4.2.3. Presence of crustal low-velocity zones associated with past and present volcanism

Crustal low-velocity zones are identified in the PG, PF and PE lines (profiles D–D', C–C' and F–F', respectively) from both our images and also raw waveform data showing either changes in S-phase amplitudes or complicated body-wave coda primarily because of different path effects (Figs. 9, 10c and S12). Such observed seismic anomalies can be closely associated with the presence of partial melt related to past or present volcanism. In particular, the imaged low velocities at the PE and PF lines (Figs. 10c and S12) can be associated with present-day volcanism because of their close proximity to active volcanoes present (Sabancaya and Chachani along the PE line; Quimsachata along the PF line). Finally, the most prominent low-velocity zone is observed in the forearc of the flat slab region along the PG line (Figs. 9 and 10c). Although this region is not coincident with current volcanism, this imaged seismic anomaly represents molten rocks related to volcanism during the steepening of the Oligocene flat slab beneath the Altiplano plateau (Ma and Clayton, 2015).

5. Conclusions

We image the Nazca Plate subduction zone system in S. Peru by relocating intra-slab earthquakes and inverting for seismic velocities. For the images, we use data from seismic arrays that were deployed to target geophysical characterization of the subduction system in the slab-dip transition zone between the flat and normally dipping segments of the Nazca Plate. Relocated seismicity from the inversion based on the double-difference method suggests a smooth contortion of the slab along the transition from 30°-to-flat-to-normal subduction. In addition, the slab elevates, following the continental Moho (Ma and Clayton, 2015), in the flat slab region, adding another force for flattening (suction) in addition to the buoyancy of the Nazca Ridge. The slab suction force plays an important role in maintaining the flat plate geometry in the vicinity of the subducting Nazca Ridge because its buoyancy alone cannot fully explain the slab-flattening process. Notable features in the inversions for the flat slab region are the relatively lower velocities for the flat slab and the high V_s and low V_p/V_s in the thin mantle layer in the backarc. The lower slab velocities suggest that the subduction of the Nazca Ridge retards the phase transition to a denser mineral (e.g., eclogite), and contributes to the buoyancy of the flat slab. An observed high V_s and low V_p/V_s in the thin mantle layer above the flat slab at ~60–85 km in depth may reflect cool conditions and possible chemical alteration via slab-derived fluids, as evidenced in the Chilean flat-slab region. The interaction of slab-derived fluids with the overlying mantle layer influences the overall slab dynamics and the cessation of upper-plate volcanism in the flat slab region.

Acknowledgements

We acknowledge Creative-Pioneering Researchers Program through Seoul National University (SNU SRnD 3345-20160014), and the Nuclear Safety Research Program through the Korea Foundation of Nuclear Safety (KoFONS), granted financial resource from the Nuclear Safety and Security Commission (NSSC), Republic of Korea (No. 1705010). We thank Editor Miaki Ishii and reviewers for comments that greatly improved this paper.

Appendix A. Supplementary material

Supplementary material related to this article can be found online at <https://doi.org/10.1016/j.epsl.2018.07.014>.

References

- Abers, G., van Keeken, P., Hacker, B., 2017. The cold and relatively dry nature of mantle forearcs in subduction zones. *Nat. Geosci.* 10, 333–337. <https://doi.org/10.1038/ngeo2922>.
- Antonijevic, S.K., Wagner, L.S., Kumar, A., Beck, S.L., Long, M.D., Zandt, G., Tavera, H., Condori, C., 2015. The role of ridges in the formation and longevity of flat slabs. *Nature* 524, 212–215. <https://doi.org/10.1038/nature14648>.
- Beck, S.L., Zandt, G., Wagner, L.S., 2010. Central Andean Uplift and the Geodynamics of the High Topography. International Federation of Digital Seismograph Networks, OtherSeismNet Network. https://doi.org/10.7914/SN/ZG_2010.
- Bilek, S.L., 2010. Seismicity along the South American subduction zone: review of large earthquakes, tsunamis, and subduction zone complexity. *Tectonophysics* 495, 2–14. <https://doi.org/10.1016/j.tecto.2009.02.037>.
- Bird, P., 2003. An updated digital model of plate boundaries. *Geochem. Geophys. Geosyst.* 4, 1027. <https://doi.org/10.1029/2001GC000252>.
- Bishop, B.T., Beck, S.L., Zandt, G., Wagner, L., Long, M., Antonijevic, S.K., Kumar, A., Tavera, H., 2017. Causes and consequences of flat-slab subduction in southern Peru. *Geosphere* 13, 1392–1407. <https://doi.org/10.1130/GES01440.1>.
- Cahill, T., Isacks, B.L., 1992. Seismicity and shape of the subducted Nazca Plate. *J. Geophys. Res.* 97 (B12), 17,503–17,529. <https://doi.org/10.1029/92JB00493>.
- Chlieh, M., Perfettini, H., Tavera, H., Avouac, J.-P., Remy, D., Nocquet, J.-M., Rolandone, F., Bondoux, F., Gabalda, G., Bonvalot, S., 2011. Interseismic coupling and seismic potential along the Central Andes subduction zone. *J. Geophys. Res.* 116 (B12405). <https://doi.org/10.1029/2010JB008166>.
- Currie, C.A., Hyndman, R.D., 2006. The thermal structure of subduction zone back arcs. *J. Geophys. Res., Solid Earth* 111. <https://doi.org/10.1029/2005JB004024>.
- Dougherty, S.L., Clayton, R.W., 2014. Seismic structure in southern Peru: evidence for a smooth contortion between flat and normal subduction of the Nazca Plate. *Geophys. J. Int.* 200 (1), 534–555. <https://doi.org/10.1093/gji/ggu415>.
- Eakin, C.M., Long, M.D., Beck, S.L., Wagner, L.S., Tavera, H., Condori, C., 2014. Response of the mantle to flat slab evolution: insights from local S splitting beneath Peru. *Geophys. Res. Lett.* 41, 3438–3446. <https://doi.org/10.1029/2014GL059943>.
- Gudmundsson, Ó., Sambridge, M., 1998. A regionalized upper mantle (RUM) seismic model. *J. Geophys. Res.* 103 (B4), 7121–7136. <https://doi.org/10.1029/97JB02488>.
- Hacker, B.R., Abers, G.A., Peacock, S.M., 2003. Subduction factory 1. Theoretical mineralogy, densities, seismic wave speeds, and H_2O contents. *J. Geophys. Res.* 108 (B1), 2029. <https://doi.org/10.1029/2001JB001127>.
- Hacker, B.R., Abers, G.A., 2012. Subduction factory 5: unusually low Poisson's ratios in subduction zones from elastic anisotropy of peridotite. *J. Geophys. Res., Solid Earth* 117, B06308. <https://doi.org/10.1029/2012JB009187>.
- Hampel, A., 2002. The migration history of the Nazca Ridge along the Peruvian active margin: a re-evaluation. *Earth Planet. Sci. Lett.* 203, 665–679. [https://doi.org/10.1016/S0012-821X\(02\)00859-2](https://doi.org/10.1016/S0012-821X(02)00859-2).
- Hasegawa, A., Sacks, I.S., 1981. Subduction of the Nazca plate beneath Peru as determined from seismic observations. *J. Geophys. Res.* 86 (B6), 4971–4980. <https://doi.org/10.1029/JB086iB06p04971>.
- Hayes, G.P., Wald, D.J., Johnson, R.L., 2012. Slab1.0: a three-dimensional model of global subduction zone geometries. *J. Geophys. Res.* 117 (B01302). <https://doi.org/10.1029/2011JB008524>.
- Hyndman, R.D., Peacock, S.M., 2003. Serpentization of the forearc mantle. *Earth Planet. Sci. Lett.* 212, 417–432. [https://doi.org/10.1016/S0012-821X\(03\)00263-2](https://doi.org/10.1016/S0012-821X(03)00263-2).
- Kennett, B.L.N., Engdahl, E.R., Buland, R., 1995. Constraints on seismic velocities in the Earth from travel times. *Geophys. J. Int.* 122, 108–124. <https://doi.org/10.1111/j.1365-246X.1995.tb03540.x>.
- Kim, Y., Clayton, R.W., Asimow, P.D., Jackson, J.M., 2013. Generation of talc in the mantle wedge and its role in subduction dynamics in central Mexico. *Earth Planet. Sci. Lett.* 384, 81–87. <https://doi.org/10.1016/j.epsl.2013.10.006>.
- Kim, Y., Clayton, R.W., Asimow, P.D., Jackson, J.M., 2015. Generation of talc in the mantle wedge and its role in subduction dynamics in central Mexico. *Earth Planet. Sci. Lett.* 429, 81–87. <https://doi.org/10.1016/j.epsl.2013.10.006>.
- Kim, Y., Clayton, R.W., 2015. Seismic properties of the Nazca oceanic crust in southern Peruvian subduction system. *Earth Planet. Sci. Lett.* 429, 110–121. <https://doi.org/10.1016/j.epsl.2015.07.055>.
- Kumar, A., Wagner, L.S., Beck, S.L., Long, M.D., Zandt, G., Young, B., Tavera, H., Miyazawa, E., 2016. Seismicity and state of stress in the central and southern Peruvian flat slab. *Earth Planet. Sci. Lett.* 441, 71–80. <https://doi.org/10.1016/j.epsl.2016.02.023>.
- Laske, G., Masters, G., Ma, Z., Pasyanos, M., 2013. Update on CRUST1.0—a 1-degree global model of Earth's crust. *Geophys. Res. Abstr.*, 20132658abstrEGU.
- Lomax, A., Satriano, C., Vassallo, M., 2012. Automatic picker developments and optimization: FilterPicker—a robust, broadband picker for real-time seismic monitoring and earthquake early warning. *Seismol. Res. Lett.* 83 (3), 531–540. <https://doi.org/10.1785/gssrl.83.3.531>.
- Ma, Y., Clayton, R.W., Tsai, V.C., Zhan, Z., 2013. Locating a scatterer in the active volcanic area of Southern Peru from ambient noise cross-correlation. *Geophys. J. Int.* 192, 1332–1341. <https://doi.org/10.1093/gji/ggs103>.
- Ma, Y., Clayton, R.W., 2014. The crust and uppermost mantle structure of Southern Peru from ambient noise and earthquake surface wave analysis. *Earth Planet. Sci. Lett.* 395, 61–70. <https://doi.org/10.1016/j.epsl.2014.03.013>.
- Ma, Y., Clayton, R.W., 2015. Flat slab deformation caused by interplate suction force. *Geophys. Res. Lett.* 42. <https://doi.org/10.1002/2015GL065195>.
- Manea, V.C., Manea, M., Ferrari, L., Orozco-Esquível, T., Valenzuela, R., Husker, A., Kostoglodov, V., 2017. A review of the geodynamic evolution of flat slab subduction in Mexico, Peru, and Chile. *Tectonophysics* 695, 27–52. <https://doi.org/10.1016/j.tecto.2016.11.037>.
- Myers, S.C., Johannesson, G., Hanley, W., 2007. A Bayesian hierarchical method for multiple-event seismic location. *Geophys. J. Int.* 171, 1049–1063. <https://doi.org/10.1111/j.1365-246X.2007.03555.x>.
- O'Driscoll, L.J., Richards, M.A., Humphreys, E.D., 2012. Nazca–South America interactions and the late Eocene–late Oligocene flat-slab episode in the central Andes. *Tectonics* 31. <https://doi.org/10.1029/2011TC003036>.
- Peacock, S.M., 2004. Thermal structure and metamorphic evolution of subducting slabs. In: Eiler, J. (Ed.), *Inside the Subduction Factory*. American Geophysical Union, Washington, D.C.
- PeruSE, 2013. Peru subduction experiment. Caltech. Dataset. <https://doi.org/10.7909/C3H41PBZ>.
- Phillips, K., Clayton, R.W., Davis, P., Tavera, H., Guy, R., Skinner, S., Stubailo, I., Audin, L., Aguilar, V., 2012. Structure of the subduction system in southern Peru from seismic array data. *J. Geophys. Res.* 117 (B11306). <https://doi.org/10.1029/2012JB009540>.
- Phillips, K., Clayton, R.W., 2014. Structure of the subduction transition region from seismic array data in southern Peru. *Geophys. J. Int.* 196, 1889–1905. <https://doi.org/10.1093/gji/ggt504>.

- Porter, R., Gilbert, H., Zandt, G., Beck, S., Warren, L., Calkins, J., Alvarado, P., Anderson, M., 2012. Shear wave velocities in the Pampean flat-slab region from Rayleigh wave tomography: implications for slab and upper mantle hydration. *J. Geophys. Res.* 117 (B11301). <https://doi.org/10.1029/2012JB009350>.
- Qian, W., Wang, W., Zou, F., Wu, Z., 2018. Elasticity of orthoenstatite at high pressure and temperature: implications for the origin of low VP/Vs zones in the mantle wedge. *Geophys. Res. Lett.* 45, 665–673. <https://doi.org/10.1002/2017GL075647>.
- Ramos, V.A., Cristallini, E., Pérez, D.J., 2002. The Pampean flat-slab of the Central Andes. *J. South Am. Earth Sci.* 15, 59–78. [https://doi.org/10.1016/S0895-9811\(02\)00006-8](https://doi.org/10.1016/S0895-9811(02)00006-8).
- Ramos, V.A., Folguera, A., 2009. Andean flat-slab subduction through time. *Geol. Soc. (Lond.) Spec. Publ.* 327, 31–54. <https://doi.org/10.1144/SP327.3>.
- Ryan, J., Beck, S., Zandt, G., Wagner, L., Minaya, E., Tavera, H., 2016. Central Andean crustal structure from receiver function analysis. *Tectonophysics* 682, 120–133. <https://doi.org/10.1016/j.tecto.2016.04.048>.
- Scire, A., Zandt, G., Beck, S., Long, M., Wagner, L., Minaya, E., Tavera, H., 2016. Imaging the transition from flat to normal subduction: variations in the structure of the Nazca slab and upper mantle under southern Peru and northwestern Bolivia. *Geophys. J. Int.* 204, 457–479. <https://doi.org/10.1093/gji/ggv452>.
- Syracuse, E.M., Abers, G.A., 2006. Global compilation of variations in slab depth beneath arc volcanoes and implications. *Geochem. Geophys. Geosyst.* 7 (Q05017). <https://doi.org/10.1029/2005GC001045>.
- Tovich, A., Schubert, G., Luyendyk, B.P., 1978. Mantle flow pressure and the angle of subduction: non Newtonian corner flows. *J. Geophys. Res.* 83 (B12), 5892–5898. <https://doi.org/10.1029/JB083iB12p05892>.
- Wagner, L.S., Beck, S., Zandt, G., Ducea, M.N., 2006. Depleted lithosphere, cold, trapped asthenosphere, and frozen melt puddles above the flat slab in central Chile and Argentina. *Earth Planet. Sci. Lett.* 245, 289–301. <https://doi.org/10.1016/j.epsl.2006.02.014>.
- Wagner, L.S., Anderson, M.L., Jackson, J.M., Beck, S.L., Zandt, G., 2008. Seismic evidence for orthopyroxene enrichment in the continental lithosphere. *Geology* 36, 935–938. <https://doi.org/10.1130/G25108A.1>.
- Waldbauer, F., Ellsworth, W.L., 2000. A double-difference earthquake location algorithm: method and application to the northern Hayward fault. *Bull. Seismol. Soc. Am.* 90, 1353–1368. <https://doi.org/10.1785/0120000006>.
- Ward, K.M., Zandt, G., Beck, S.L., Wagner, L.S., Tavera, H., 2016. Lithospheric structure beneath the northern Central Andean Plateau from the joint inversion of ambient noise and earthquake-generated surface waves. *J. Geophys. Res., Solid Earth* 121, 8217–8238. <https://doi.org/10.1002/2016JB013237>.
- Yuan, X., Sobolev, S.V., Kind, R., Oncken, O., Bock, G., Asch, G., Schurr, B., Graeber, F., Rudloff, A., Hanka, W., 2000. Subduction and collision processes in the Central Andes constrained by converted seismic phases. *Nature* 408, 958–961. <https://doi.org/10.1038/35050073>.
- Zhang, H., Thurber, C.H., 2003. Double-difference tomography: the method and its application to the Hayward fault, California. *Bull. Seismol. Soc. Am.* 93 (5), 1875–1889. <https://doi.org/10.1785/0120020190>.